Modeling and analysis of compaction-induced traveltime shifts for multicomponent seismic data

Steven Shawn Smith[1] and Ilya Tsvankin[1]

ABSTRACT

Modeling of time shifts associated with time-lapse (4D) seismic surveys is helpful in evaluating reservoir depressurization and inverting for subsurface stress. Using coupled geomechanical and full-waveform seismic modeling, we study the influence of compaction-induced stress and strain around a simplified reservoir on compressional (P), shear (S), and mode-converted (PS) waves. We estimate compaction-induced time shifts and analyze their dependence on reflector depth and pressure drop inside the reservoir. Time shifts between synthetic baseline and monitor surveys are obtained by processing techniques that are potentially applicable to field data. Although P-wave time-shift lags for reflectors in the overburden are indicative of induced anisotropy, they are two to three times smaller than S-wave time-shift leads for reflectors beneath the reservoir. We also investigate the contributions of the deviatoric and volumetric stains to the time shifts for all three modes. Time shifts for S- and PS-waves are strongly influenced by elevated volumetric and deviatoric strains inside the reservoir. Almost constant S-wave time shifts for a range of offsets and source locations indicate that the contribution of stress-induced velocity anisotropy to shear-wave signatures is weak because the symmetry is close to elliptical. Our modeling also shows that mild tilt of a rectangular reservoir, or its replacement with an elliptically shaped reservoir of the same aspect ratio, has little influence on time shifts. Potentially, the developed methodology can be applied to estimate compaction-induced stress fields using simple compartmentalized reservoir models.

INTRODUCTION

Pore-pressure reduction inside a producing reservoir causes compaction, as well as strain, stress, and impedance changes within the reservoir and in the surrounding rock. These changes can manifest themselves through surface subsidence and major damage or disruption of drilling operations and infrastructure (McCann and Wilts, 1951; Geertsma, 1973; Strehle, 1987; Guilbot and Smith, 2002; Barkved and Kristiansen, 2005; Scott, 2007; Sayers, 2010). These geomechanical changes produce traveltime and amplitude variations that are visible in seismic data, and can be exploited to monitor oil and gas production (Lumley, 1995; 2001; Guilbot and Smith, 2002; Hatchell and Bourne, 2005; Calvert, 2005). Time-lapse seismic data can provide information about fluid movement (drainage), reservoir compaction, compartmentalization, and hydraulic fracturing or flooding (injection) processes during production. The associated time shifts can potentially be inverted for the pressure distribution in the reservoir and induced stress field throughout the medium (McCann and Wilts, 1951; Landrø, 2001; Sayers et al., 2002; Hodgson et al., 2007). Time-lapse methods may also be applied to reservoirs experiencing pressure increase during CO_2 sequestration (Lumley et al., 2008).

Previous research based on geomechanical and seismic methods includes two main directions. One of them focuses on zero-offset time-lapse data governed by vertical stress/strain (Landrø and Stammeijer, 2004; Hatchell and Bourne, 2005; Roste, 2007), while the other considers a full triaxial stress field (Herwanger et al., 2007; Sayers and Schutjens, 2007; Scott, 2007; Herwanger and Horne, 2009; Fuck et al., 2009). Whereas the approach based on vertical strain helps evaluate compaction limits, horizontal and shear stress/strain are also induced during production, generating a heterogeneous, anisotropic velocity field inside and around the reservoir. Thus, accurate modeling of prestack time shifts should involve the complete triaxial stress/strain field, which

accounts for both volumetric (compactional) and deviatoric (shear) strain.

Compaction-induced stress and strain are computed by integrating a "strain nucleus" over the reservoir volume (McCann and Wilts, 1951; Downs and Faux, 1995; Hu, 1989), or by finite-element modeling. The response of the reservoir rock matrix and pore fluids to confining (overburden) pressure is governed by the empirically determined effective stress (Biot-Willis) coefficient (Hofmann et al., 2005; Schutjens et al., 2004; Zoback, 2007). Computation of stress/strain-related stiffnesses for time-lapse seismic modeling requires empirical values of the third-order stiffness coefficients, as described by the nonlinear theory of elasticity (Hearmon, 1953; Sarkar et al., 2003; Prioul et al., 2004).

Fuck et al. (2009, 2011) analyze stress/strain-induced anisotropy and P-wave time shifts in 2D models using a linearized perturbation of reflection traveltimes and verify their results by performing anisotropic ray tracing. In particular, they show that the offset dependence of P-wave time shifts is governed primarily by induced anisotropy, and that the symmetry axis deviates from the vertical only in areas of large shear strain near the reservoir corners. Thus, the symmetry of most of the section is close to vertical transverse isotropy (VTI).

Here, we use geomechanical simulation and full-waveform elastic seismic modeling to investigate stress/strain-induced time shifts for a simplified reservoir that undergoes changes in effective pressure. Each code solves its own set of partial differential equations (PDEs), which is referred to as "semi-coupled" modeling (Olden et al., 2001; Minkoff et al., 2004; Sen and Settari, 2005; Dusseault et al., 2007). We start by discussing the background theory and modeling algorithms and then introduce a methodology for measuring time shifts
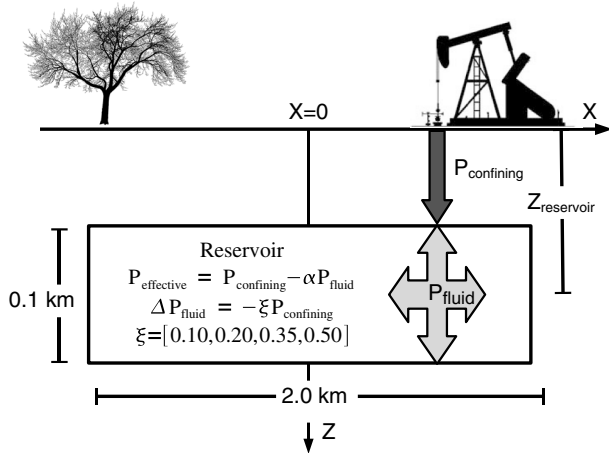

Figure 1. Reservoir geometry after Fuck et al. (2009). Pore-pressure ($P_P = P_{\text{fluid}}$) reduction occurs only within the reservoir, resulting in an anisotropic velocity field due to the excess stress and strain. For geomechanical modeling, the reservoir is located in a model space measuring $20 \text{ km} \times 10 \text{ km}$, which is sufficient for obtaining stress, strain, and displacement close to those for a half-space. The reservoir is comprised of and embedded in homogeneous Berea sandstone ($V_P = 2300 \text{ m/s}$, $V_S = 1456 \text{ m/s}$, $\rho = 2140 \text{ kg/m}^3$) with the following density-normalized third-order stiffness coefficients: $C_{111}/\rho = -13,904 \text{ GPa}$, $C_{112}/\rho = 533 \text{ GPa}$, and $C_{155}/\rho = 481 \text{ GPa}$ (Prioul et al., 2004). The Biot coefficient (α) for the reservoir is 0.85. Velocities in the model are reduced by 10% from the laboratory values to account for the difference between static and dynamic stiffnesses in low-porosity rocks (Yale and Jamieson, 1994).

between baseline and monitor survey shot records. The time-shift estimation algorithms have been developed for both synthetic and field data. Our processing workflow is used to study time shifts of P-, S-, and PS-waves for a wide range of reservoir depths and effective pressure reductions. In particular, S-wave time shifts are shown to be largely controlled by changes in the shear-wave vertical velocity within the reservoir, and PS-wave time shifts are strongly raypath-dependent. Finally, we estimate the contributions of deviatoric and volumetric strains to the time shifts and evaluate the influence of mild changes in reservoir shape and tilt on time-lapse signatures.

THEORETICAL BACKGROUND

To study time-lapse multicomponent wavefields for compacting reservoirs, we estimate time shifts from waveforms created by elastic seismic modeling preceded by finite-element computations of induced displacement, stress, and strain. For simplicity, the methodology is implemented for a single-compartment reservoir model of varying pressure, depth, shape, and dip. Typical reservoir geometry and properties are illustrated in Figure 1. A rectangular reservoir shape simulates a simplest-case scenario, such as a fault-bound, relay-ramp block trap in a rift system, similar to Heidrun field in the North Sea (Whitley, 1992).

Compaction-induced displacement, stress, and strain are computed using COMSOL PDE software (COMSOL AB, 2008). The reservoir is made up of homogeneous Berea sandstone, in which pore-pressure (P_P) reduction causes a change in the effective pressure (P_{eff}) of the system (Hofmann et al., 2005; Schutjens et al., 2004; Zoback, 2007). Pressure inside the reservoir (P_{res}) that counteracts the confining pressure of the overburden (P_{over}) is comprised of rock-matrix and fluid components:

$$P_{\text{res}} \simeq P_{\text{fluid}} + P_{\text{matrix}} \simeq \alpha P_P, \quad (1)$$

where α is the effective stress coefficient (i.e., the Biot-Willis coefficient for dry rock), and

$$\alpha = 1 - \frac{K_a}{K_g}; \quad (2)$$

K_a is the aggregate bulk modulus of the rock frame and fluids, and K_g is the bulk modulus of the grain material (Zoback, 2007); typical values of α for Berea sandstone range between 1.0 and 0.6 (Sarker and Batzle, 2008). Therefore, the influence of the rock matrix on the pore-pressure change is governed by the effective stress coefficient, and drops in pore pressure are attributed to the pore fluid ($\Delta P_P \approx \Delta P_{\text{fluid}}$). The effective reservoir pressure governing displacement, strain, and stress across the section is given by:

$$P_{\text{eff}} = P_{\text{over}} - \alpha P_{\text{fluid}}. \quad (3)$$

Initially, the system is assumed to be in hydrostatic equilibrium, with the reservoir pressure balancing that of the homogeneous overburden column:

$$P_{\text{res}} = P_{\text{over}}, \quad (4)$$

$$\left(1 - \frac{K_a}{K_g}\right) P_P = \alpha P_P = \rho_{\text{over}} \, g \, z_{\text{res}}. \quad (5)$$

For our homogeneous sandstone model, compaction is relatively small and confined primarily to the reservoir, but stress and strain in the surrounding rock cause non-negligible changes in stiffness. As verified by Fuck et al. (2009), the resulting stress/strain fields for a depressurizing rectangular inclusion are close to analytic solutions obtained by Hu (1989).

Following Fuck et al. (2009), compaction-induced changes in the stiffness coefficients of the medium are computed from the geomechanical strains using the nonlinear theory of elasticity which operates with the third-order stiffness coefficients, c_{ijklmn} (Prioul et al., 2004). An expression for strain-induced stiffness changes is derived from the second- and third-order terms of the nonlinear strain-energy function (Hearmon, 1953). The perturbations of the second-order stiffnesses c_{ijkl} as a function of the excess strain tensor Δe_{mn} are described by:

$$c_{ijkl} = c_{ijkl}^0 + \frac{\partial c_{ijkl}}{\partial e_{mn}} \Delta e_{mn} = c_{ijkl}^0 + c_{ijklmn} \Delta e_{mn}, \quad (6)$$

where c_{ijkl}^0 are the stiffnesses of the background (unstressed) medium. In the Voigt matrix notation (e.g., Tsvankin, 2005), equation 6 can be written as (Fuck and Tsvankin, 2009)

$$C_{\alpha\beta} = C_{\alpha\beta}^0 + C_{\alpha\beta\gamma} \Delta e_\gamma. \quad (7)$$

Equation 6 linearizes the changes in stiffness with respect to excess strain. Our modeling employs the third-order stiffness coefficients ($C_{\alpha\beta\gamma}$) measured by Sarkar et al. (2003). The stress/strain-induced changes in the stiffnesses c_{ijkl} described by equations 6 and 7 result in a heterogeneous, anisotropic velocity field around the compacting reservoir. Compaction-induced triaxial stress applied to the initially isotropic medium produces a heterogeneous model with orthorhombic symmetry (Tsvankin, 2005; Fuck and Tsvankin, 2009). In 2D the medium is transversely isotropic with a tilted symmetry axis (TTI); the symmetry of the stressed medium is studied in detail by Fuck and Tsvankin (2009).

Wave propagation in the perturbed medium can be modeled using Hooke's law:

$$s_{ij} = c_{ijkl} e_{kl}, \quad (8)$$

where **s** and **e** are the stress and strain tensors (denoted by **s** and **e** to avoid confusion with the anisotropy parameters σ and ε). Application of equations 6 and 7 to a purely isotropic unstressed medium yields the second-order stiffnesses of the stressed medium as a function of two independent third-order stiffness coefficients, C_{111} and C_{112} (Fuck et al., 2009). The compaction-induced stiffness changes are used to model the elastic wavefield of the 4D (monitor) survey. If ray tracing is employed, the resulting time shifts can be expressed as "isotropic" traveltimes computed along reference rays in the background medium plus perturbations caused by the variation of the stiffness coefficients along the same raypaths (Fuck et al., 2009).

Reductions in effective reservoir pressure, which are monotonic and linear (equation 3), are used as the forcing functions for the constitutive and Navier equations that govern induced displacement, stress, strain and, therefore, changes in the stiffness coefficients.

METHODOLOGY

Modeling

To obtain compaction-induced displacements, stresses, and strains corresponding to those of a half-space, we model the geomechanics of the reservoir and surrounding medium using a finite-element mesh that is 10 times larger than the reservoir itself (Figure 1). The top of the model is a free surface, while the other three sides are clamped, zero-displacement boundaries. These conditions allow accurate modeling of geomechanics near the reservoir while permitting surface subsidence.

Pore-fluid pressure reductions of 10%, 20%, 35%, and 50% of the initial fluid pressure span a plausible range (up to 70%) for oil and gas reservoirs. We assume that the pore fluid is "dead" oil, which does not undergo phase changes during depressurization. Therefore, oil/gas phase transitions ("bubble points") are not modeled, and the bulk modulus inside the reservoir varies only with numerically modeled ΔP_{eff}, stress, and strain (Batzle and Han, 2009). Our modeling algorithms compute changes in the stiffness coefficients, but we do not attempt any additional simulation of cracks, porosity changes, fluid movement, plastic or brittle deformation, or failure associated with stress applied to the pore space (Christensen and Wang, 1985; Prasad and Manghnani, 1997; Shapiro, 2003; Fjær, 2009). However, the difference between the confining and effective pressure for our sandstone-based models does not exceed 30 MPa, placing them below a typical point of material failure (Fjær, 2009). Because of this, and of negligible compaction in our models, the rock material described by strain-induced stiffnesses is considered to be linear and elastic (Schutjens et al., 2004; Scott, 2007), but includes inherent properties of the laboratory samples used by Sarkar et al. (2003) to determine the third-order stiffness coefficients.

The spatial distribution of the compaction-induced stress and strain may be complex, depending on the geologic structure and properties of the reservoir and background. However, for reasonably simple horizontally layered media, the impact of background heterogeneity around the reservoir on stresses and time shifts is generally not pronounced (Fuck et al., 2011). Additional complexity, not accounted for in our current models, may be caused by significant reservoir heterogeneity. For example, reservoir tilt can result in distinct separation of brine and liquid/gas hydrocarbons into multiple pore spaces (compartments) with different bulk moduli.

For the baseline ($\Delta P = 0$) and monitor ($\Delta P > 0$) surveys, multicomponent seismic data are generated using a fourth-order elastic finite-difference code (Sava et al., 2010) with an 8 m × 8 m grid spacing to propagate waves with frequencies up to 40 Hz. This grid spans a 6 km × 3 km region around the reservoir (with individual reservoirs located at five depths ranging from 0.5 km to 2.5 km). The wavefield is excited by a vertical point force that generates both P-waves and in-plane polarized S-waves (i.e., SV-waves); the source signal is the Ricker wavelet with a central frequency of 10 Hz. To simplify isolation and processing of reflections used for time-shift measurements, we apply absorbing boundary conditions at all sides of the model. This reduces ground roll and unphysical reflections caused by an improperly implemented free-surface condition in the finite-difference code (see below). For each source location and drop in reservoir pressure, we model reflections individually from 22 interfaces at depths ranging between 0.2 km and

3.0 km (i.e., "sample" the Green's function between the source and receivers for a set of hypothetical reflection points along each interface). The reflectors are not included in the geomechanical modeling so that they do not perturb the modeled strain/stiffness fields caused by reduction in P_{eff}. Each reflector is inserted as a single-grid-point horizontal interface of high density (8000 kg/m^3).

This density contrast ensures that the generated reflections are sufficiently strong compared to those due to pressure (impedance) changes in the reservoir (Figures 2a, 2c, and 3a). For each reflector depth, time shifts for P-waves are estimated from vertical-component shot records, whereas S- and PS-time shifts are measured on the horizontal component.

Figure 2. X-component (horizontal displacement) shot records illustrating removal of artifact reflections with contrasting and similar slopes. Polarities of traces located to the right of the source are reversed during processing to ensure left/right time-shift symmetry. Here, the desired reflection is the PS-wave arrival. The first few milliseconds of parts (a) and (c) have been zeroed to improve visualization of later arrivals. (a) Baseline ($\Delta P = 0$) survey shot record containing P-, PS-, and S-wave arrivals for a measurement reflector at approximately 1.6 km depth. (b) PS-wave from plot (a) following windowing and F-K filtering of an artifact reflection with contrasting slope. (c) Monitor survey shot record with reflections from the reservoir caused by change in reservoir impedance due to pressure drop ($\Delta P = 20\%$). These events have slopes similar to that of the PS reflection at 2600 ms. (d) PS arrival following windowing and unsuccessful f-k filtering of reservoir reflections.
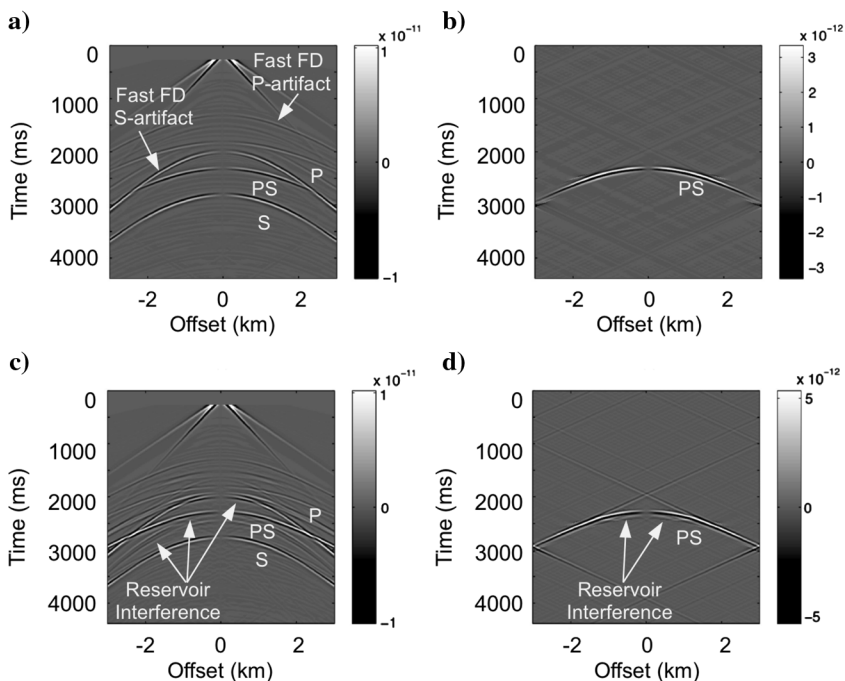

Figure 3. (a) X-component monitor shot record with interfering events for $\Delta P = 20\%$ and a source at $X = 2$ km. The PS event of interest is masked by high-amplitude reflections from the reservoir with both contrasting and similar slopes. (b) PS-wave time-shift curve (solid line) with cross-correlation skips for traces 90–150 resulting in a time-shift artifact for the 21st-order polynomial fit (dashed). (c) Same time-shift curve (solid) after cross-correlation skip prevention with improved polynomial fit (dashed).
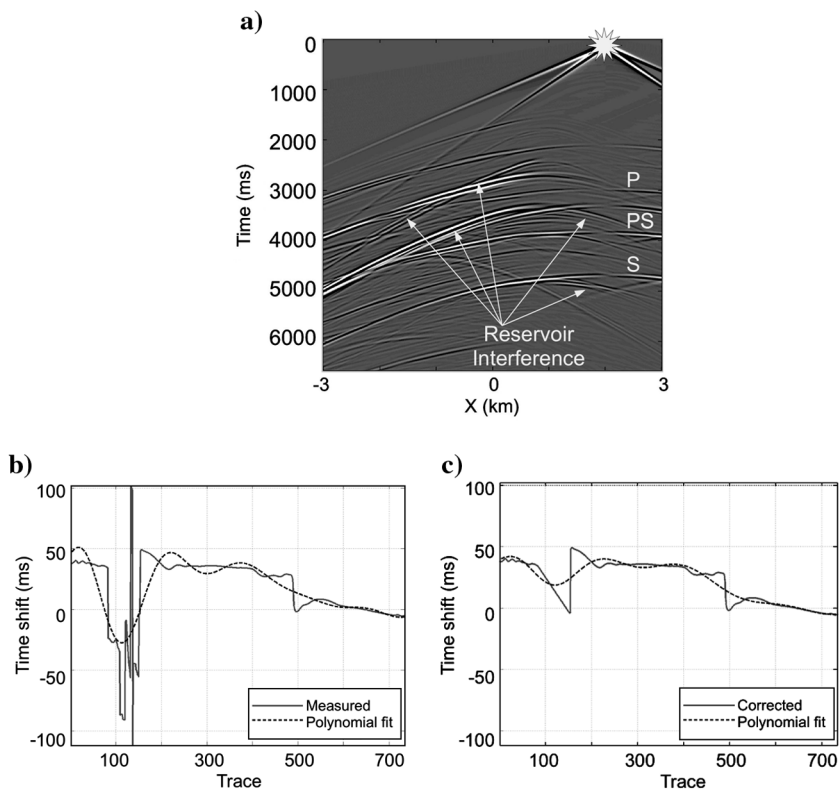
Estimation of time shifts

Accurate measurements of time shifts from seismic data are necessary for constructing time-shift curves and surfaces, and ultimately inverting the time-lapse signatures for subsurface stress. For each reflector (see above), we implement cross-correlations between windowed arrivals from baseline and monitor survey traces to obtain smooth time-shift curves as a function of offset. Therefore, it is desirable that the wavelets from the baseline and monitor surveys have similar characteristics. This can be achieved by cross-equalization techniques on field data (e.g., Rickett and Lumley, 2001), but is implemented here for synthetic data by filtering out additional reflections caused by changing reservoir impedance.

Our synthetic data contain two types of events that interfere with measurement reflections and distort the wavelet shapes. In a controlled modeling environment, the density of the reflectors may simply be increased to enhance the events of interest, but that approach cannot be applied to field data. First, the finite-difference modeling code generates unphysical reflections from the top boundary of the model. These artifacts have the appearance of regular, high-velocity reflections in both baseline and monitor shot records and intersect events of interest with contrasting slopes. Figure 2a shows such a fast-moving S-wave artifact interfering with PS-wave arrivals in a baseline survey shot gather. Arrivals with such large, dissimilar slopes are removed using velocity-based *f-k* filtering of shot records, as illustrated in Figure 2b. The presence of numerical artifacts is fortuitous when considering and designing time-shift measurement algorithms, as similar interference may be present in field data, or for models with greater structural complexity.

The second type of undesired reflections that distort wavelets on monitor survey records is caused by impedance changes inside the reservoir following a pressure drop. The slopes and traveltimes of these reservoir reflections may be close to those of the events of interest for a wide range of offsets (Figure 2c). Due to this interference, time delays associated with the maximum cross-correlation value between the baseline and monitor wavelets can vary rapidly from trace to trace, resulting in a discontinuous ("skylined") time-shift curve. Because *f-k* processing is incapable of separating events with similar slopes (Figure 2d), additional processing is required.

Contamination by reservoir reflections is even more substantial when the source is moved away from the center of the reservoir (Figure 3a). An estimated time-shift curve exhibiting cross-correlation skips caused by this interference is shown in Figure 3b. Such skips in a segment of this time-shift curve exceed 200 ms; in some cases, multiple discontinuous sections can occur. Smoothing this curve with a high-order polynomial (or low-pass filter) results in a strongly distorted, oscillating time-shift function. To mitigate this problem, we apply an algorithm that repeatedly sweeps the time-shift curve at small to large length scales and smooths out discontinuous segments (Figure 3c). Still, in some cases, jumps may remain after flattening, and parts of the time-shift curve may not be suitable for time-lapse analysis (see Figure 10c–10f, $X \lesssim -0.8$ km, $Z \approx 2.0 - 2.5$ km).

Following *f-k* filtering and the skip-prevention procedure, each time-shift curve is sequentially fitted with polynomials of increasing order. A curvature-based ("L-curve") selection criterion is applied to the residuals between the measured time shifts and the polynomial fit. The maximum curvature of the residual as a function of polynomial order determines the optimal fit. This method retains the dominant time-shift trends without fitting small-scale jumps or discontinuities left over from the previous processing steps. Time-shift surfaces (Figures 8–10 and 12–15) are constructed by a cubic-spline interpolation of a full set of processed time-shift "hull" curves from each reflector, similar to those in Figure 3c.

Additional interference and geometry-related issues may occur with field data, requiring further enhancement/cross-equalization of arrivals used for computing time shifts. Depending on the
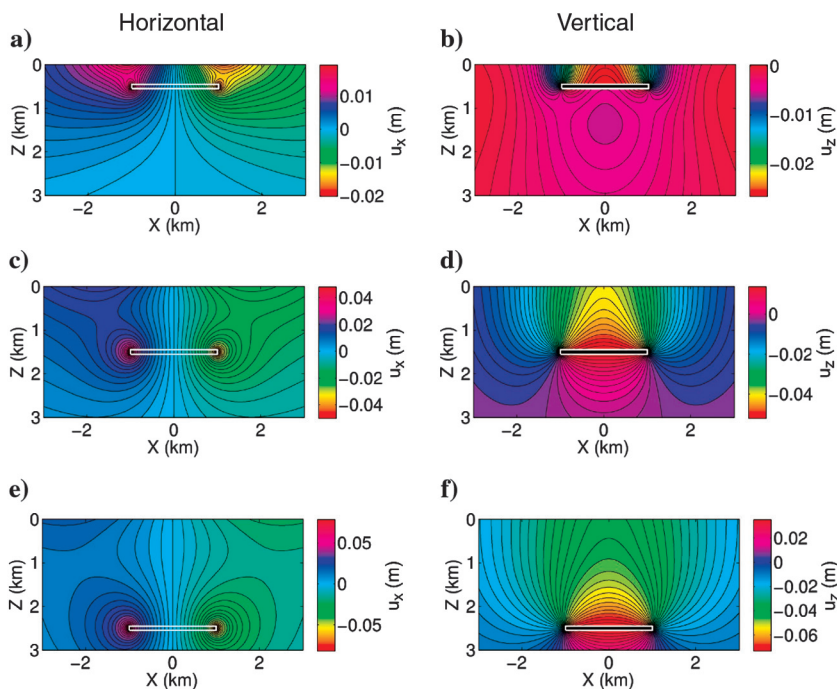

Figure 4. Compaction-induced horizontal (a, c, and e) and vertical (b, d, and f) displacement components for the reservoir (white box) at depths of (a, b) 0.5 km, (c, d) 1.5 km, and (e, f) 2.5 km. Note that although depth increases downward, the axis of vertical displacement points up.

Smith and Tsvankin

Figure 5. Strains computed for rectangular (a, c, e) and elliptical (b, d, f) reservoirs of similar aspect ratios located at 1.5 km depth; $\Delta P = 20\%$. (a, b) Horizontal strain e_{11}, (c, d) vertical strain e_{33}, and (e, f) shear strain e_{13}. The plots show the part of the section used for finite-difference modeling.
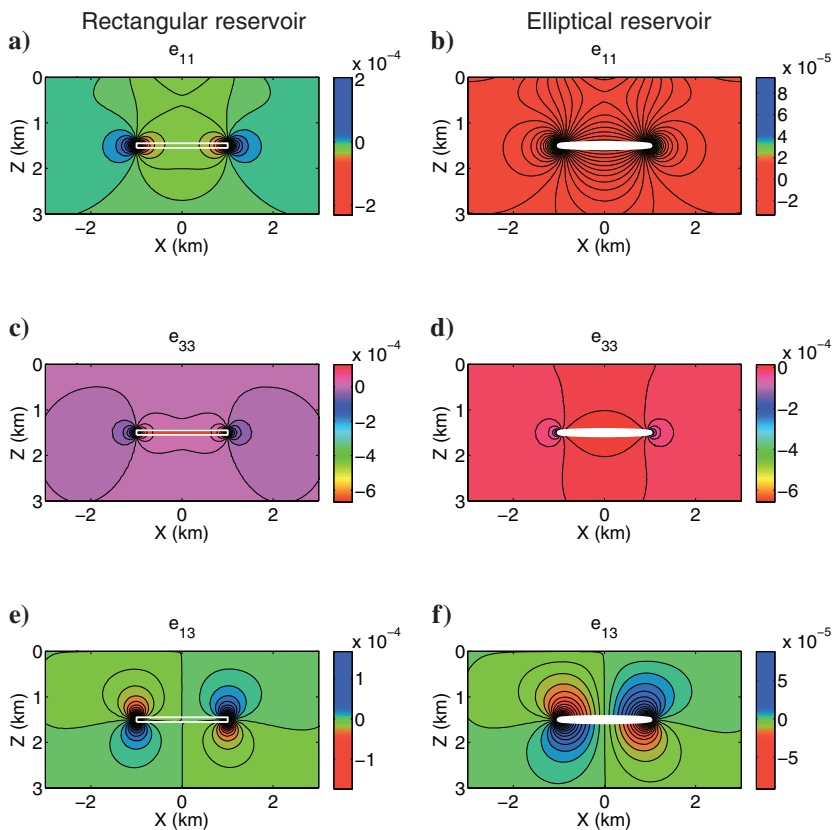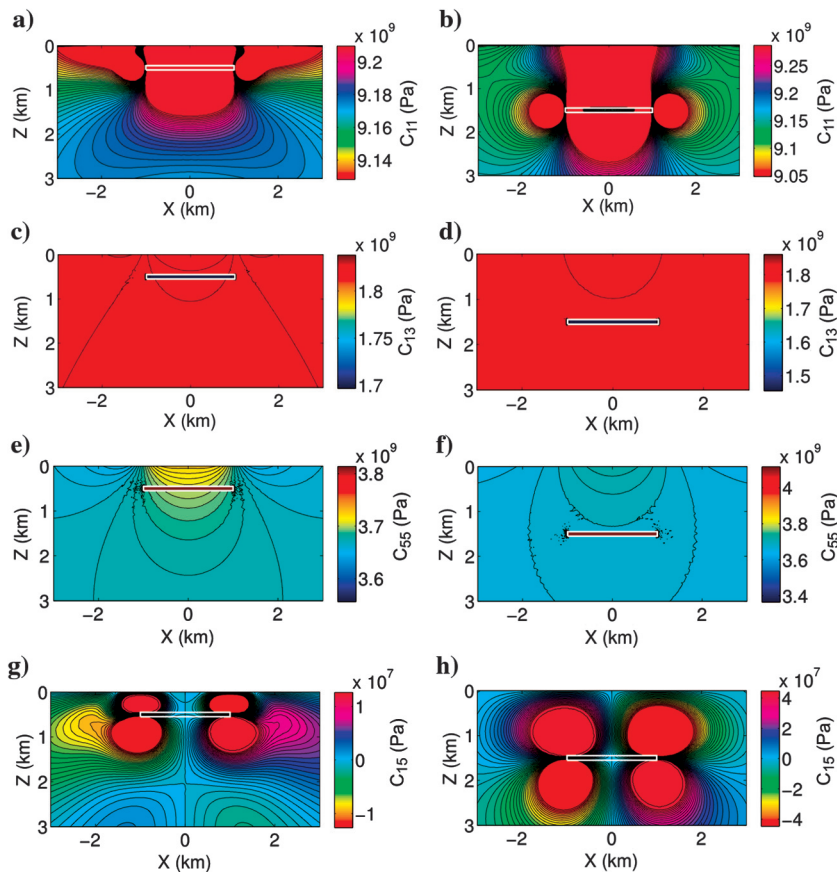

Figure 6. Stiffness coefficients (a, b) C_{11}, (c, d) C_{13}, (e, f) C_{55}, and (g, h) C_{15}, for reservoir depths of (a, c, e, g) 0.5 km and (b, d, f, h) 1.5 km; $\Delta P = 20\%$. The structure of C_{33} is similar to that of C_{13}, with significant values largely confined to the reservoir. C_{11} and C_{15} have been clipped and smoothed.
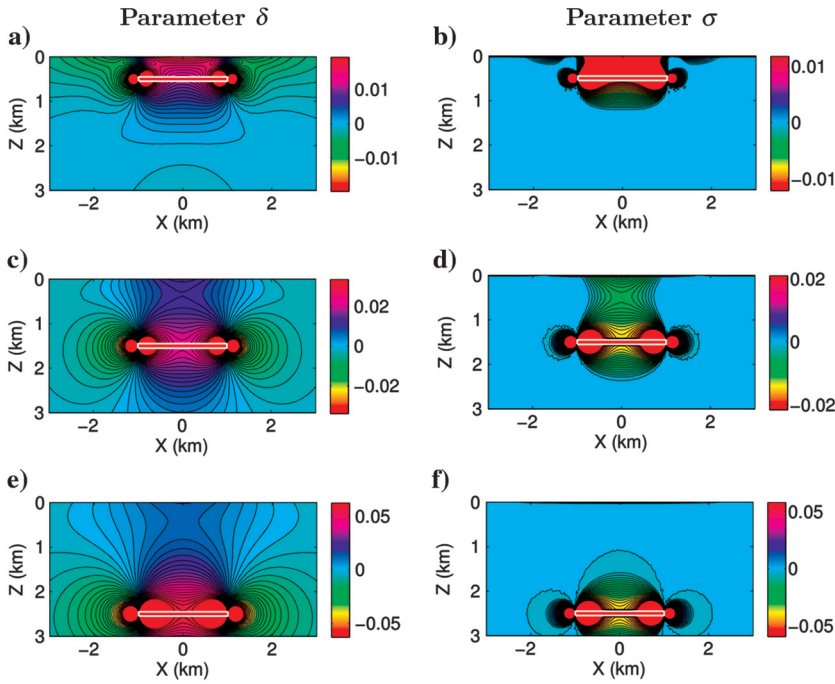
Figure 7. Spatial distributions of the anisotropy parameters δ (left column) and σ (right column, equation 9) for reservoirs at (a, b) 0.5 km, (c, d) 1.5 km, and (e, f) 2.5 km depth and $\Delta P = 20\%$. The maps have been clipped at three standard deviations for visualization purposes, and the number of contour lines is identical for all plots.
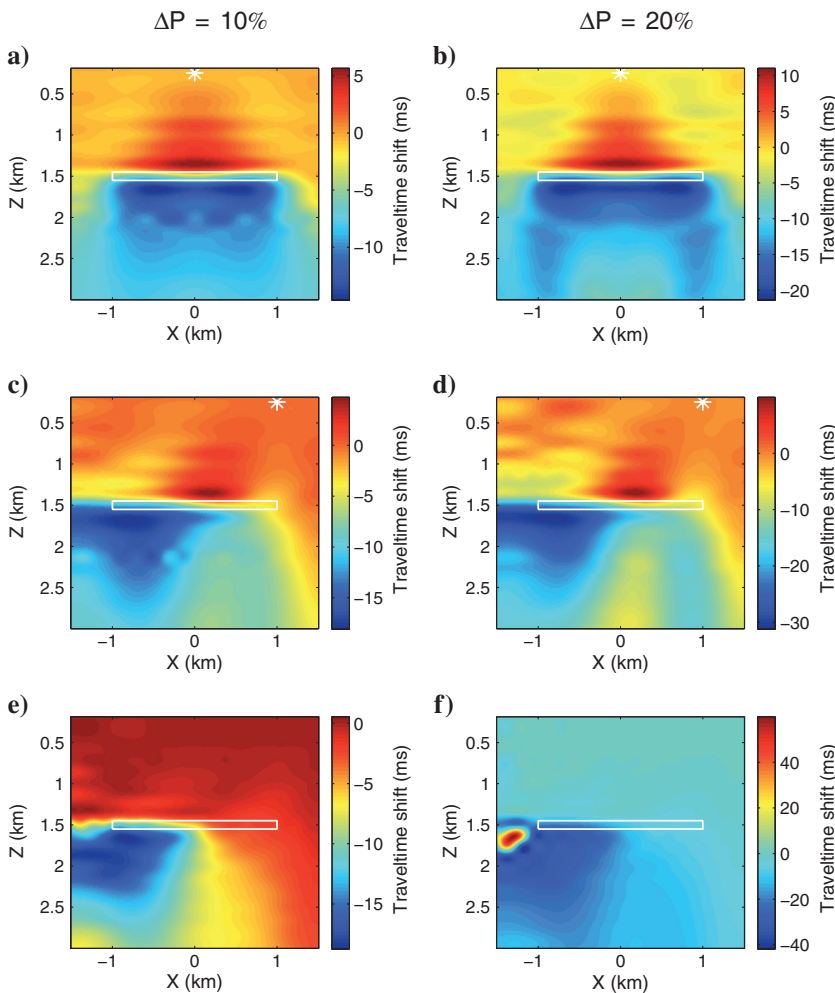

Figure 8. P-wave time shifts for the model in Figure 1 for a shot (white asterisk) located at (a, b) $X_0 = 0$ km, (c, d) $X_0 = 1$ km, and (e, f) $X_0 = 2$ km (outside the plot). The time shift shown at each (X, Z) point corresponds to the reflection from a horizontal interface at depth Z recorded at the source-receiver offset $2(X - X_0)$, where X_0 is the source coordinate. Pore-pressure drops are 10% for (a, c, e) and 20% for (b, d, f).

geologic properties of the section, both reflectors and layers may deform substantially during compaction, and shifts computed from such arrivals may be distorted by geometric changes. However, for stiff materials similar to our sandstone model, compaction is small and confined primarily to the reservoir (Figure 4), making any geometry-related time shifts negligible.

ANALYSIS OF MODELING RESULTS

Geomechanical and anisotropy variations with depth

The spatial distribution of the excess stress/strain across the section is a function of the reservoir dimensions, elastic properties, proximity to the free surface, and the stiffness contrast between the reservoir and the background (Fuck et al., 2011). Compaction-induced displacements, strains, and stiffnesses exhibit the largest spatial variations when the reservoir is close to the free surface (Figures 4–7). In our models, at reservoir depths exceeding 1.5 km, the influence of the free surface is diminished and the spatial distribution of geomechanical parameters approaches that for a whole space.

The in-plane displacements are shown in Figure 4 for a range of reservoir depths. The spatial variations of the horizontal displacements shrink to small regions around the endcaps with increasing reservoir depth. The near-surface displacement anomaly results in

the well-known surface "subsidence bowl" (McCann and Wilts, 1951; Geertsma, 1973; Strehle, 1987; Zoback, 2007). Vertical displacement (compaction) increases with reservoir depth and includes the development of a "pull-up zone" beneath the reservoir (Figure 4f).

Large horizontal strain values (Figure 5) are confined to the reservoir endcaps, with shear strains showing a vertical bipolar pattern. Therefore, while the reservoir is vertically compressed, the endcaps are "pinched out." For elliptically shaped reservoirs the shear strains are distributed ("splayed") across the top and bottom reservoir interfaces (Figure 5f). The spatial distribution of the strains remains consistent for the entire range of reservoir depths, but varies in magnitude. Strain magnitudes (and corresponding stresses) at the corners of the rectangular reservoir are exaggerated due to its sharp corners. Similar stress/strain fields have been modeled by Dusseault et al. (2007) and Fuck et al. (2009, 2011), and the strain magnitudes in Figure 5 agree with those cited by Barton (2006) for reservoir compaction. The stress/strain fields of elliptical reservoirs (see below), while not substantially different from those of rectangular reservoirs, may be more realistic.

The stiffness coefficients C_{11}, C_{13}, C_{15}, and C_{55}, which serve as input to the finite-difference code, are shown in Figure 6 for two reservoir depths. The fields of C_{11} and C_{55} are clipped and smoothed to reduce numerical singularities at the reservoir corners.

Figure 9. S-wave time shifts for the model in Figure 1 (same display as in Figure 8) for a shot located at (a, b) $X_0 = 0$, (c, d) $X_0 = 1$ km, and (e, f) $X_0 = 2$ km.
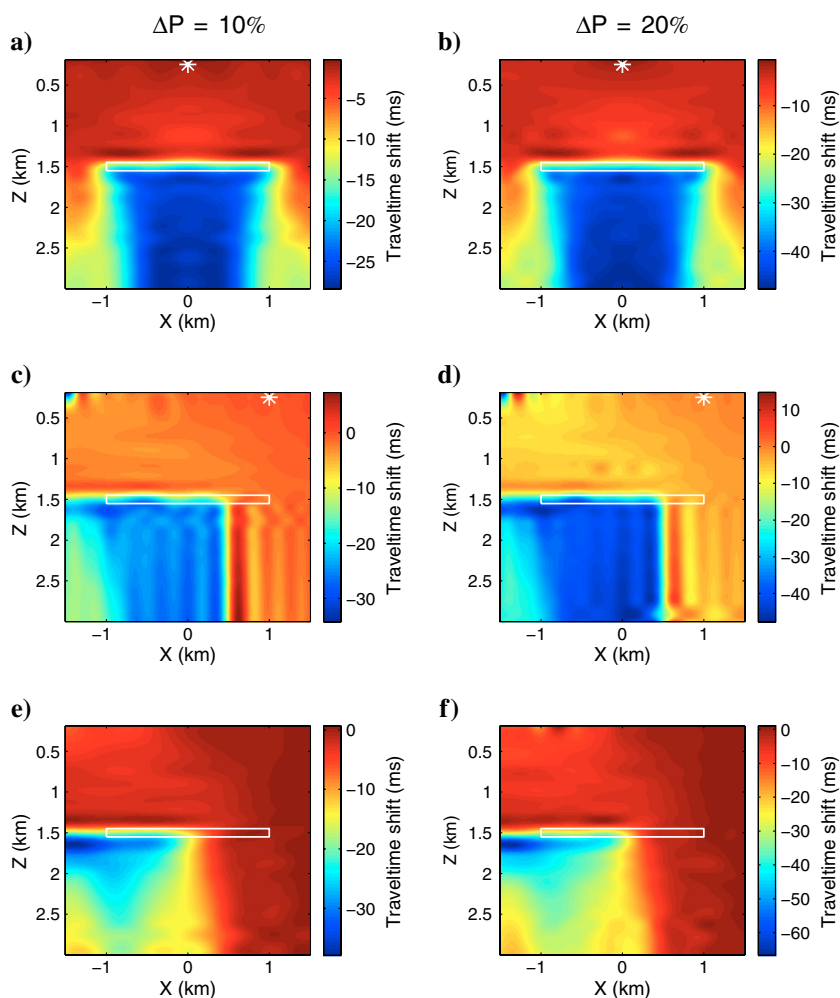
Similar to C_{13} and C_{55}, the most significant values of C_{33} (not shown) are confined to the reservoir volume. The spatial distribution and magnitude of C_{35} are similar to those of C_{15}, with both stiffnesses being approximately two orders of magnitude smaller than the other coefficients, resulting in a medium close to VTI. Only in regions at the sharp corners of the reservoir, anomalously large values of C_{15} and C_{35} cause a substantial tilt of the symmetry axis (Fuck et al., 2009; see Figure 6).

The anisotropy parameters δ (Figure 7) and ε are computed directly from the stiffness coefficients (Tsvankin, 2005). In agreement with the results of Fuck et al. (2009), δ is non-negligible throughout the model, with the largest values near the reservoir endcaps. The spatial variation of δ is largely responsible for the offset dependence of P-wave time shifts above and to the sides of the reservoir, which is clearly visible in Figure 8a and 8b (Fuck et al., 2009). For our model, $\delta \approx \varepsilon$ and the stress-induced anisotropy is approximately elliptical, in agreement with many published results (e.g., Shapiro, 2003; Fuck et al., 2009).

While compaction-induced velocity anisotropy causes time shifts with respect to an isotropic background, any traveltime variations caused by the presence of an intrinsically anisotropic layer, such as shale, will be present in the baseline survey. Because reservoir shape, depth, P_{eff}, and stiffness contrast with the background

are the primary controls of the induced stress/strain field (Fuck et al., 2011), any additional compaction-induced time shifts due to such an intrinsically anisotropic layer will be negligible.

Time shifts for rectangular reservoirs

Time-shift maps for P-, S-, and PS-waves produced by interpolating between hull curves (Figure 3b and 3c) are displayed in Figures 8, 9, and 10. The time shifts correspond to hypothetical specular reflection points at each (X, Z) location in the subsurface. Negative shifts are referred to as "leads" because the event from the monitor survey arrives earlier than the corresponding event from the baseline survey, while positive time shifts are referred to as "lags." Figure 11 shows the largest time shifts as a function of reservoir depressurization and depth for each wave type (P, PS, and S), picked separately for regions above and below the reservoir. For a few cases, estimated time shifts were close to zero or their spatial distribution was not sufficiently smoothed by the post-processing. Then picked values of the maximum time shifts were ignored and the trend was computed using a surface-fitting algorithm. Consequently, some large time shifts, particularly those for maximum reservoir depth and depressurization, may be artificially high. Time shifts for field data recorded near reservoir corners (edges) may be
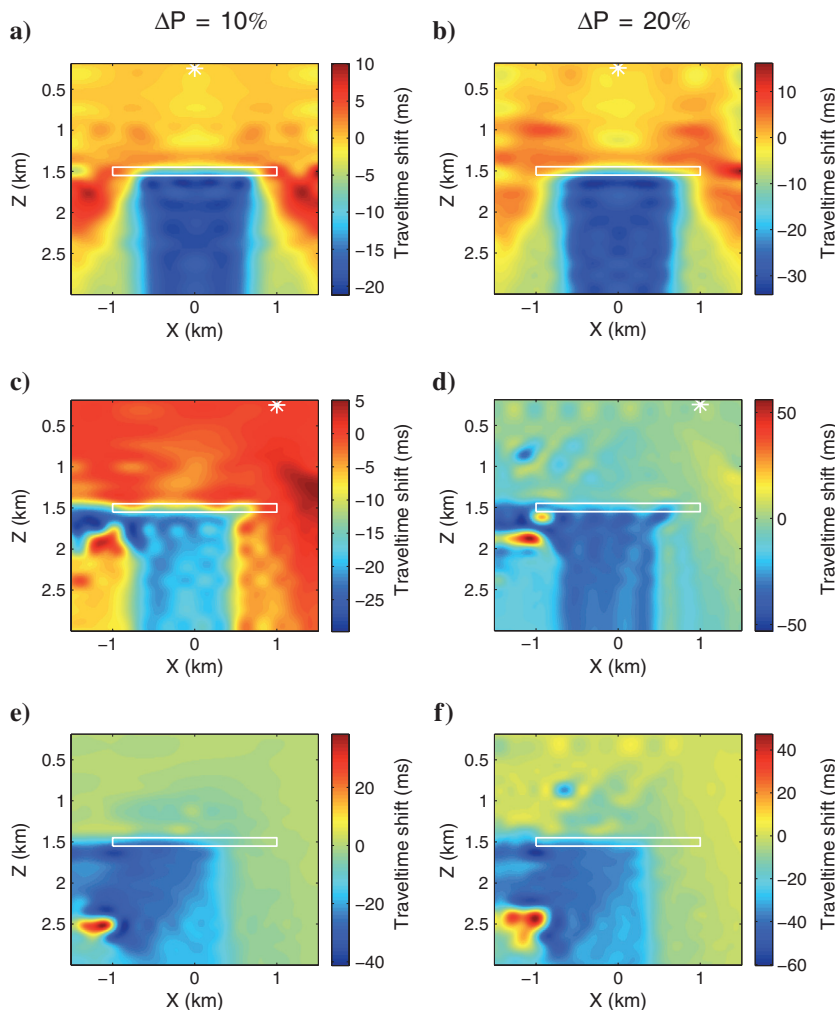

Figure 10. PS-wave time shifts for the model in Figure 1 (same display as in Figure 8) for a shot located at (a, b) $X_0 = 0$, (c, d) $X_0 = 1$ km, and (e, f) $X_0 = 2$ km.

smaller than those for our current model due to differences in reservoir shape (i.e., due to pinch outs), or to reduced time-shift resolution caused by processing algorithms.

P-wave time shifts (Figure 8) exhibit spatial patterns related to those of the parameter δ (Figure 7a, 7c, and 7e), with noticeable offset dependence caused primarily by stress-induced anisotropy (i.e., by δ). In agreement with the spatial distribution of δ, the offset dependence of time shift falls off with increasing lateral distance of the source from the reservoir center ($X = 0$). This effect is illustrated in Figure 8c, 8e, and 8d, 8f, where the shot is moved away from the region of compaction-induced stress and strain centered at $X = 0$. Offset dependence of time shifts is higher for receivers located between the source and the reservoir, where compaction-induced changes occur. As the source moves away from the reservoir center, the P-wave lag distribution above the reservoir tilts laterally toward the source, whereas the P-wave lead distribution below the reservoir tilts away from the source. In a manner similar to the pure lensing of S-waves (see below), rays entering the elevated velocities inside the reservoir at sufficiently high angles of incidence are refracted toward the endcaps (Figure 8c and 8d, -1.5 km $\leq X \leq -1.0$ km, $Z = Z_{\mathrm{res}}$).

Figure 8a and 8b demonstrates that for larger pore-pressure drops, the highest P-wave time-shift leads concentrate beneath the reservoir corners, where they are related to elevated deviatoric strain both above and below the reservoir (Figure 12e, below). P-wave time shifts for a pressure drop of 5 MPa (16%) are close to those obtained by Fuck et al. (2009) using linearized traveltime equations and ray tracing. For the maximum pressure drop (50%), P-wave lags reach a maximum of 45 ms above the reservoir located at 2.5 km depth; the leads below the reservoir are approximately two times smaller (Figure 11).

In contrast to P-waves, the offset dependence of the S-wave time shifts in Figure 9 is much weaker. The SV-wave velocity in TI media is primarily controlled by the anisotropy parameter σ (Tsvankin, 2005):

$$\sigma \equiv \left(\frac{V_{\mathrm{P0}}}{V_{\mathrm{S0}}}\right)^2 (\epsilon - \delta), \tag{9}$$

where V_{P0} and V_{S0} are the symmetry-direction P- and S-wave velocities. The linearized SV-wave phase velocity as a function of the phase angle θ with the symmetry axis can be written as

$$V_{\mathrm{SV}}(\theta) = V_{\mathrm{S0}}(1 + \sigma \sin^2 \theta \cos^2 \theta). \tag{10}$$

For elliptical anisotropy ($\epsilon = \delta$) $\sigma = 0$, $V_{\mathrm{SV}} = V_{\mathrm{S0}}$, and the SV-wave velocity function becomes isotropic. Here, non-negligible values of σ are confined almost entirely to the reservoir (Figure 7b,

Figure 11. Maximum time shifts of each mode as a function of reservoir depth Z_{res} and pore-pressure drop ΔP. Source is located above the center of reservoir. (a) P-waves above the reservoir, (b) P-waves below the reservoir, (c) S-waves above the reservoir, (d) S-waves below the reservoir, (e) PS-waves above the reservoir, and (f) PS-waves below the reservoir.
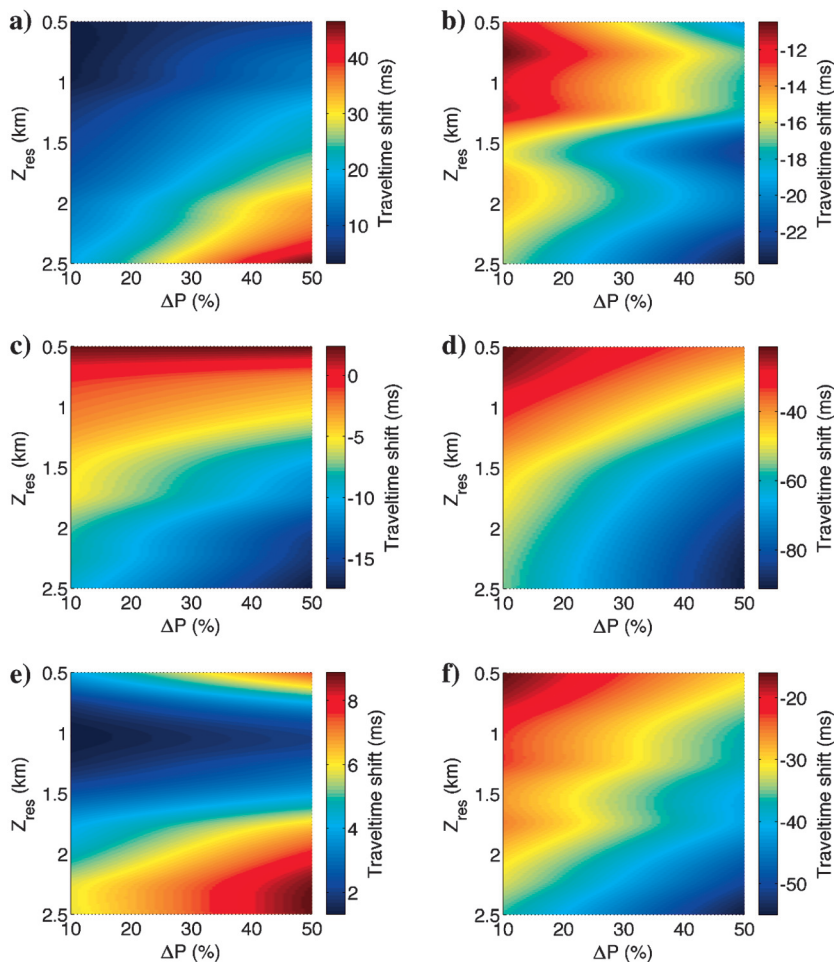
7d, and 7f). For example, when the reservoir depth is 1.5 km, the maximum absolute value of σ for a 5 MPa (16%) pressure drop is just 0.08 (σ is negative) at the center of the reservoir; for a 20 MPa (64%) pressure drop, the maximum $|\sigma|$ is 0.15. Therefore, S-wave time shifts for reflectors near and beneath the reservoir are primarily influenced by the increase in V_{S0} inside the reservoir, which reaches approximately 16% for a 5 MPa pressure drop, and 30% for a 20 MPa drop. The offset dependence of time shifts for S-waves is mostly due to the spatial distribution of V_{S0}. The large S-wave time shifts modeled here agree with rock-physics observations that shear-wave velocities are sensitive to changes in P_P, and thus P_{eff} (Xu et al., 2006).

Because the largest strains and changes in V_{S0} occur inside the reservoir, it essentially behaves like a high-velocity lens for shear waves. This is illustrated by changing S-wave time-shift patterns as the source moves away from the reservoir center (Figure 9a, 9c, 9e and 9b, 9d, 9f). Higher velocities inside the reservoir rotate incident rays toward the endcaps, while rays with small incidence angles return from reflection points beneath the reservoir (Figure 9a, 9b, 9c, 9d). As the source distance from

the center of the reservoir (and thus incident angle) increases, higher time-shift leads beneath the reservoir move laterally away from the source (Figure 9c, 9d, 9e, 9f). Time-shift leads from beneath the reservoir for S-waves (and PS-waves) are approximately two to three times those for P-waves, reaching up to 90 ms; S-wave leads above the reservoir are much smaller (Figure 11). Aside from anisotropy-induced offset dependence of time shifts, similar behavior is seen for P-waves near the endcap opposite the source (Figure 8c–8f).

PS-wave time shifts (Figure 10) represent a "mixed-mode" combination of P- and S-wave lags and leads and, therefore, strongly depend upon raypath trajectory around the reservoir. Above and to the sides of the reservoir, downgoing P-waves are influenced by the compaction-induced anisotropy. Time shifts for the upgoing S-wave from reflection points in the overburden may possess small leads due to increasing values of C_{55} (Figure 6e and 6f). These leads reduce lags accumulated along the downgoing P-raypath (Figure 9). However, the upgoing S-leg of the mode conversion remains mostly unperturbed by compaction if it does not return to the surface through the high-velocity "lens" of the reservoir. When the source
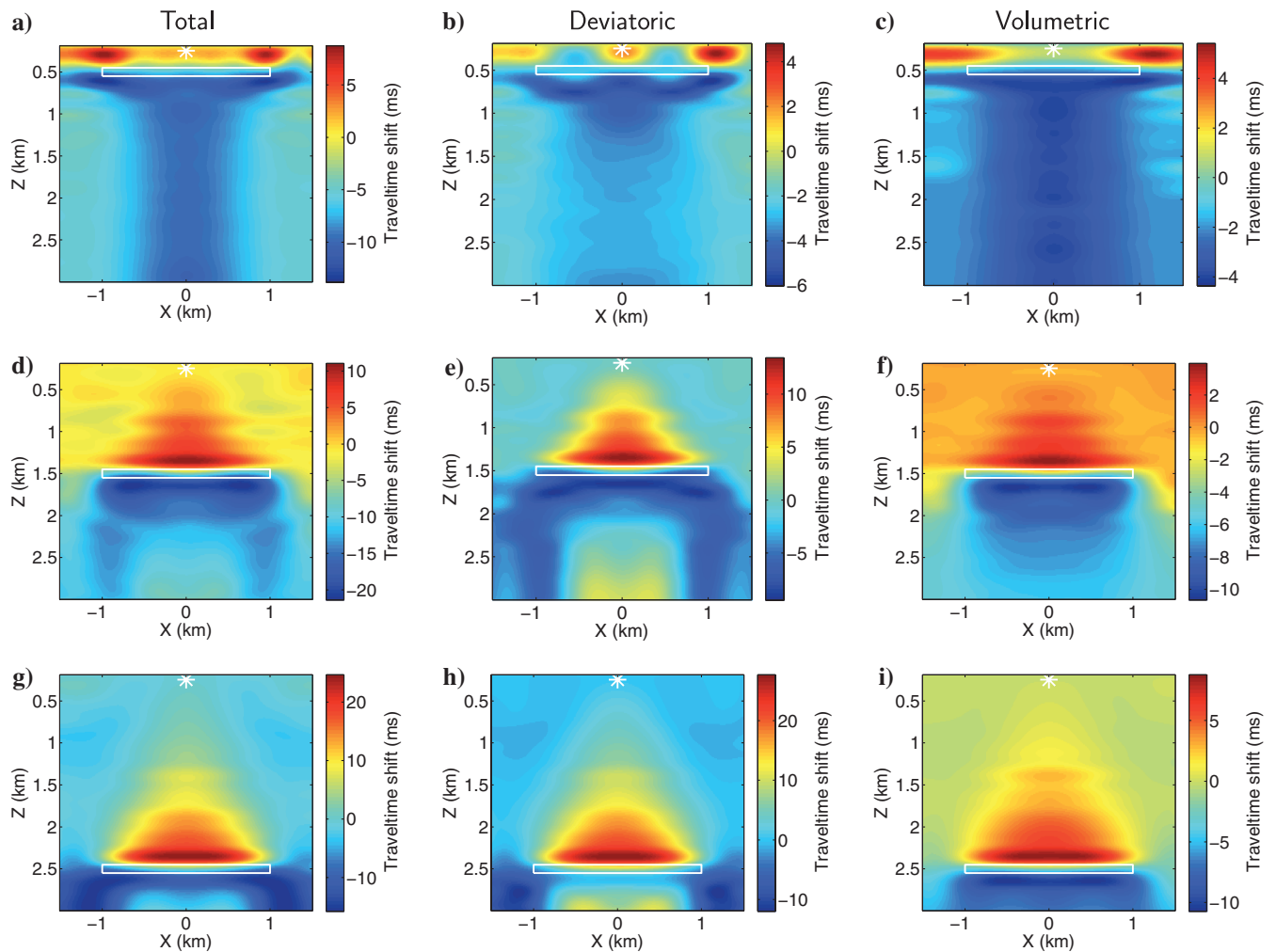

Figure 12. P-wave time shifts computed using (a, d, g) the total strain field, (b, e, h) deviatoric strain, and (c, f, i) volumetric strain. The reservoir depth is (a, b, c) 0.5 km, (d, e, f) 1.5 km, and (g, h, i) 2.5 km; $\Delta P = 20\%$.

is located above the reservoir, small-offset P-to-S conversions from deep reflectors pass through the reservoir twice, thus accumulating large time-shift leads. The offset dependence of PS-wave time shifts is clearly visible above and to the sides of the reservoir (Figure 10a and 10b). Similar to pure P-waves, the spatial distribution of time shifts in these regions varies with source location, mostly due to compaction-induced P-wave anisotropy (Figure 10a, 10c, 10e and 10b, 10d, 10f).

For all source locations, time-shift patterns for converted waves traveling through the reservoir are dominated by the increased velocities inside it, and exhibit the lensing patterns similar to those of S-waves in Figure 9. P-wave lags accumulated above the reservoir are reduced depending on the raypath and propagation time along the downgoing ray inside the reservoir, the reflection-point location, and changes in V_S due to C_{55} variations above the reservoir. Moderate leads can occur if the P-wave refracts and propagates for a sufficient distance in the higher-velocity reservoir, and converts to an S-wave and returns to the surface outside it. This lag-to-lead transition occurs at reflection points in a region below and to the sides of the reservoir. The transition from moderate to substantial leads is observed at reflection coordinates

where both the downgoing P-wave and upgoing S-wave cross the reservoir.

Contributions of volumetric and deviatoric strains

Traveltime shifts are controlled by the combined influence of the volumetric and deviatoric strains. The volumetric strain is given by one-third of the trace of the strain tensor ($\mathbf{e}$):

$$\Delta e_{kk} = \frac{1}{3}\,\mathrm{tr}(\mathbf{e}) = \frac{1}{3}\,(\Delta e_{11} + \Delta e_{22} + \Delta e_{33}). \quad (11)$$

The strain Δe_{kk} represents hydrostatic/compressive compaction and is substantial mostly inside the reservoir and near its endcaps (see Figure 5a, 5b, 5c, and 5d). Small variations in volumetric strain occur in the overburden with a distribution similar to that of C_{55} (Figure 6e and 6f). To estimate time shifts from volumetric strain, the diagonal elements of the strain tensor are assigned one-third of their geomechanically modeled values, while the off-diagonal elements are set to zero. Time shifts due to shear compaction are estimated using the deviatoric strain,
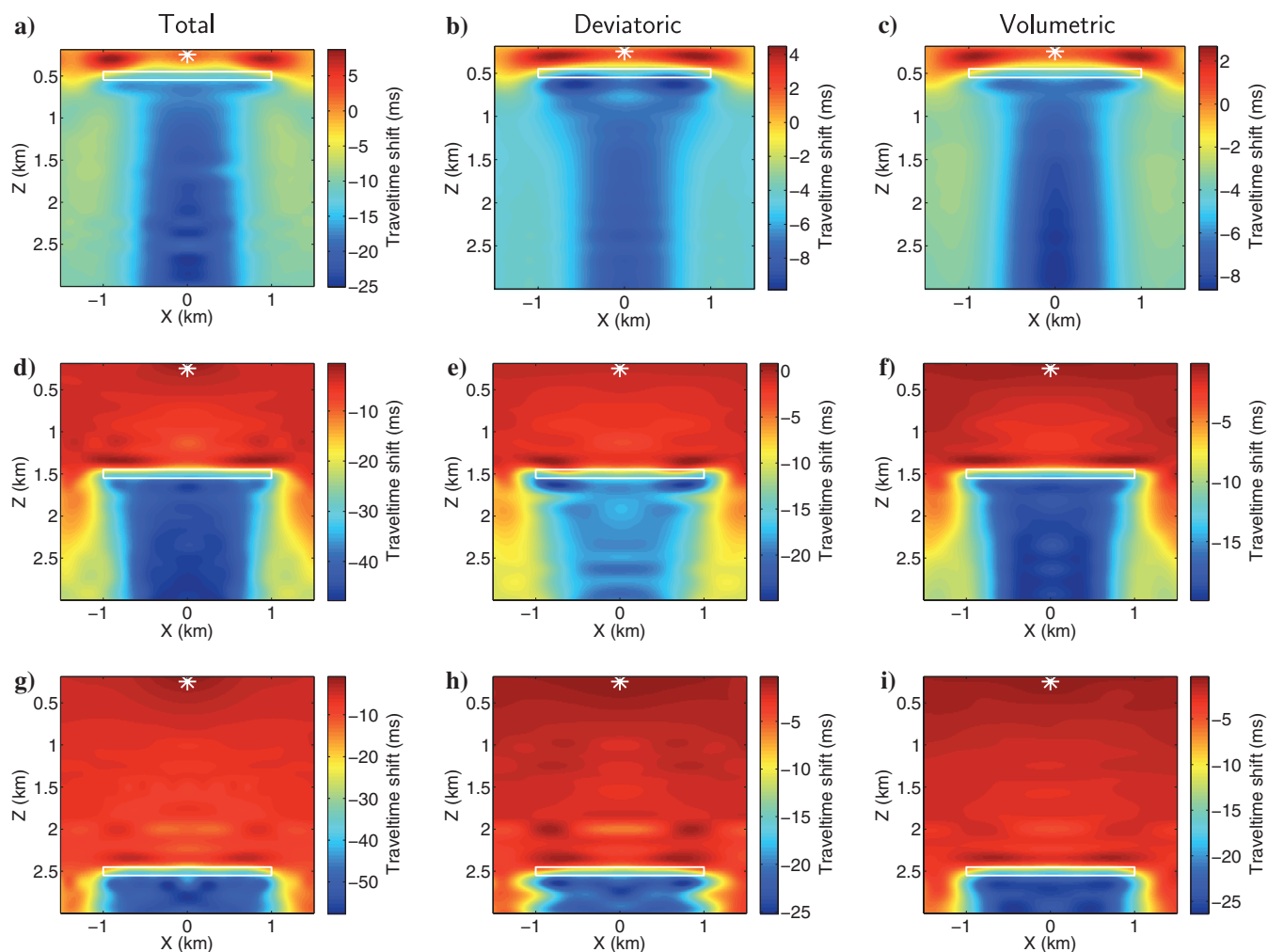

Figure 13. S-wave time shifts computed using (a, d, g) the total strain field, (b, e, h) deviatoric strain, and (c, f, i) volumetric strain. The reservoir depth is (a, b, c) 0.5 km, (d, e, f) 1.5 km, and (g, h, i) 2.5 km; $\Delta P = 20\%$.

$$\Delta \mathbf{e}_d = \mathbf{e} - \frac{1}{3} \, \mathrm{tr}(\mathbf{e}) \, \mathbf{I}, \qquad (12)$$

and is computed by subtracting one-third of the strain trace from each diagonal strain component (Davis and Selvadurai, 1996). Wellbores located in subsurface regions of high volumetric strain could snap because of compression or extensional failure, whereas wells in regions of high deviatoric strain could experience shear failure.

Figure 12 shows the contributions of the total, deviatoric, and volumetric strain to the P-wave time shifts for three reservoir depths. The deviatoric component is clearly responsible for velocity anisotropy, and thus for P-wave time-shift variation with offset outside the reservoir (Figure 12b, 12e, and 12h), particularly below the endcaps. However, the influence of deviatoric strain declines with increasing depth beneath the center of the reservoir, where the strain tensor primarily represents vertical/volumetric compaction (Figures 5 and 12c, 12f, 12i). With the exception of areas near the endcaps, the arching and "pull-up" regions immediately above and below the reservoir (Figure 4b, 4d, 4f) experience slightly higher displacements/strains than the rest of the section outside the reservoir (Figure 5c). These regions correlate with larger values of δ outside the reservoir

(Figure 7), and manifest themselves through elevated P-wave shifts at points near the reservoir (Figures 8a, 8b and 12d, 12e, 12f, 12g, 12h, 12i). In the pull-up region directly beneath the reservoir, volumetric strains contribute primarily to P-wave leads (Figure 12c, 12f, 12i). Deviatoric strains in the arching region above the reservoir are largely responsible for P-wave lags (Figure 12b, 12e, 12h).

As expected (equation 10), neither deviatoric nor volumetric strains produce significant S-wave anisotropy around the reservoir (Figure 13). With the exception of the elevated shear/deviatoric strain near the endcaps, the spatial distribution of the relatively small S-wave time shifts above the reservoir resembles that of the stiffness C_{55} (Figure 6e and 6f). At larger reservoir depths and pressures S-wave time shifts above the reservoir become significant (lags up to 17 ms, Figure 11); these larger values, produced by both volumetric (Figure 13c, 13d, 13i) and deviatoric (Figure 13b, 13e, 13h) strains, are concentrated near the collapsing endcaps. In contrast to concentrations of P-wave time shifts immediately outside the top and bottom reservoir boundaries, any elevated S-wave shifts near the reservoir boundary are confined to regions beneath the reservoir corners (Figures 5e and 13b, 13e, 13h). Below the reservoir
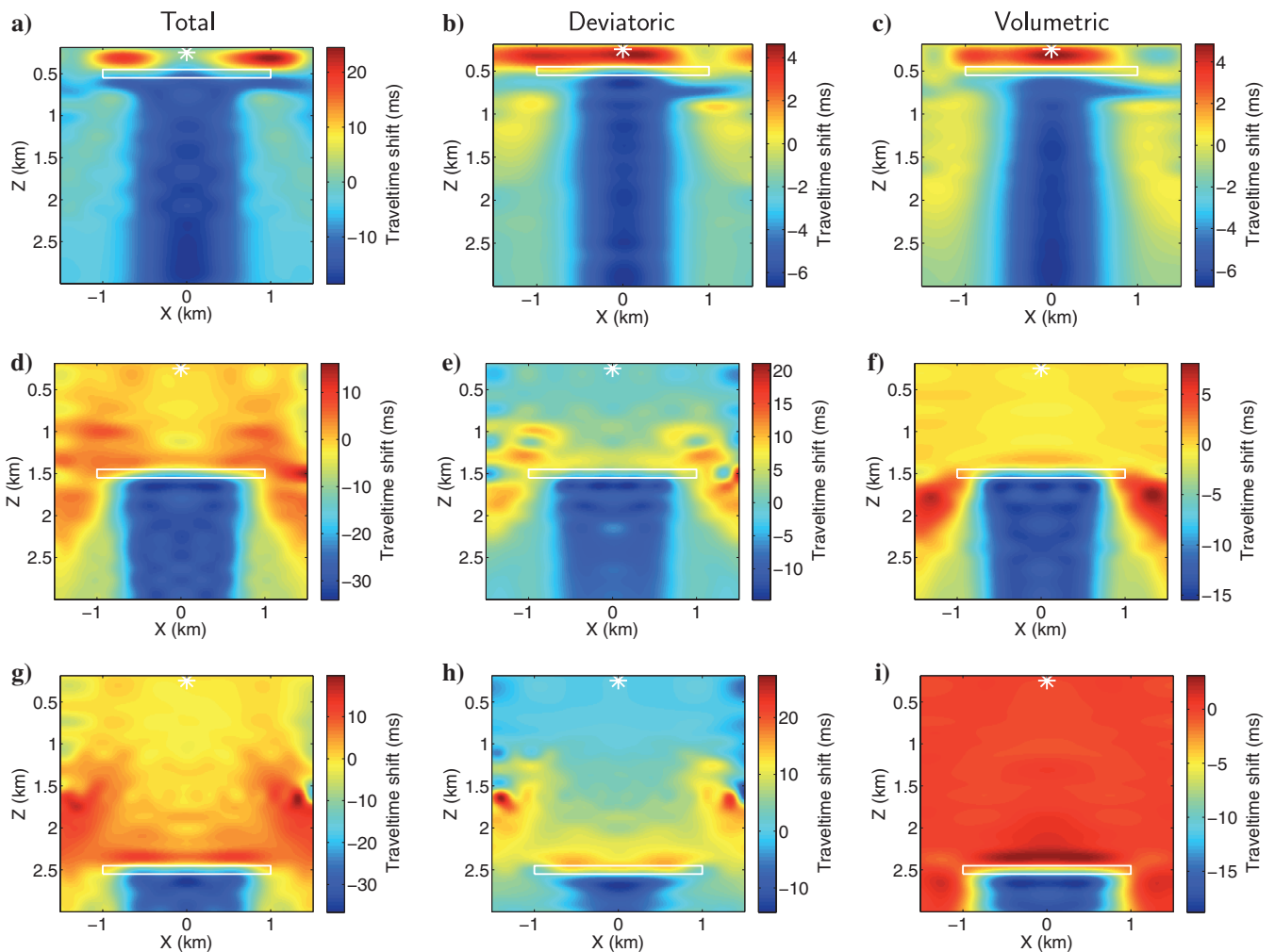

Figure 14. PS-wave time shifts computed using (a, d, g) the total strain field, (b, e, h) deviatoric strain, and (c, f, i) volumetric strain. The reservoir depth is (a, b, c) 0.5 km, (d, e, f) 1.5 km, and (g, h, i) 2.5 km; $\Delta P = 20\%$.

and away from its boundaries, volumetric and deviatoric contributions to the total S-wave time shifts are approximately equal.

The influence of volumetric and deviatoric strains on PS-wave time shifts (Figure 14) depends on whether or not the raypath intersects the elevated strain area inside the reservoir. For rays propagating above and to the sides of the reservoir, time-shift lags are incurred primarily on the downward P-wave leg. Figure 14b, 14e, and 14h confirms that the offset dependence of these time shifts is controlled by deviatoric strains (Figure 8c, 8d, 8e, 8f). Upgoing S-waves are insensitive to deviatoric strain, and propagate without accumulating any significant time shifts to the sides of the reservoir. However, small changes in C_{55} directly above the reservoir (Figure 6e and 6f) increase shear-wave velocity, which reduces PS-wave lags accumulated along the downgoing P-leg. Downgoing rays that cross the reservoir accumulate P-wave lags due to deviatoric strains, followed by a speed-up incurred inside the reservoir. As with pure S-waves, volumetric (Figure 14c, 14f, 14i) and deviatoric (Figure 14b, 14e, 14h) strains make approximately equal contributions to PS-wave time shifts for reflectors below the reservoir.

Sensitivity to reservoir shape and tilt

For the purpose of inverting for P_{eff} and the induced stress field in the overburden, it is also important to analyze the sensitivity of time shifts to perturbations of the shape and dip of individual reservoir compartments. Multicompartment reservoirs are typically modeled using several rectangular blocks. Although rectangular compartments can represent fault-block structures in rift systems, ellipses may be better suited for modeling the shapes of channels in coastal or fluvial environments, or reservoirs that "pinch-out" at their edges. Large time-shift variations caused by minor changes in shape or tilt may present problems in pressure inversion for complex/multicompartment reservoirs.

Figure 15d–15f shows P-, S-, and PS-wave time shifts for an elliptical reservoir with the same aspect ratio as the rectangular reservoir from Figure 1. The strain fields for both reservoir shapes are compared in Figure 5. The "splaying" of shear strains across the top and bottom of the elliptical reservoir results in a perturbation of the deviatoric strain field with respect to that of the rectangular reservoir. This reduces the width of the P-wave time-shift anomaly above the reservoir, and slightly widens the anomalies below the endcaps.
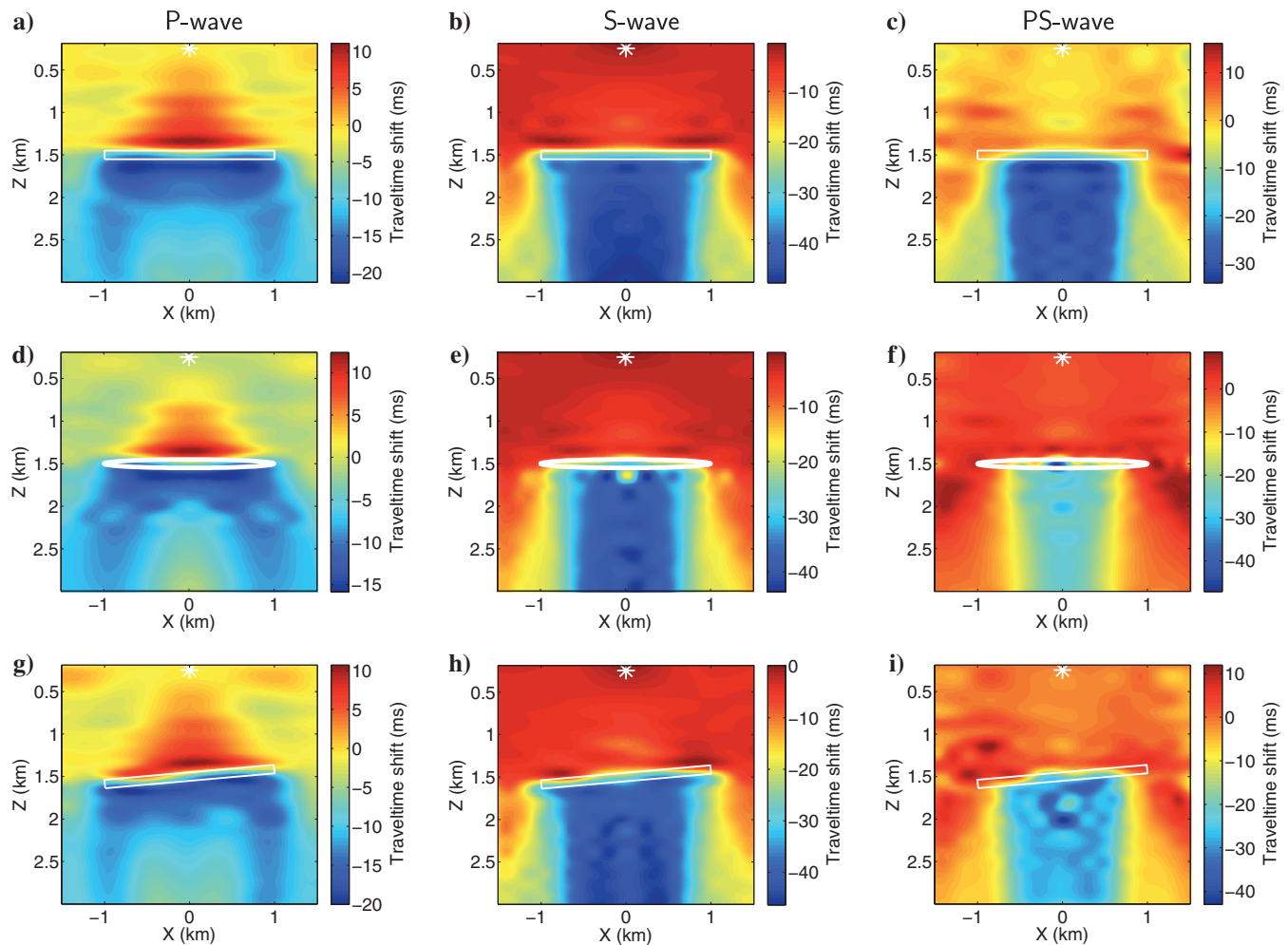

Figure 15. Influence of reservoir shape and mild tilt on the time shifts of (a, d, g) P-waves, (b, e, h) S-waves, and (c, f, i) PS-waves. (a, b, c) Horizontal rectangular reservoir, (d, e, f) elliptical reservoir of the same aspect ratio, and (g, h, i) rectangular reservoir tilted by 5° (same display as in Figure 8).

The width of the PS- and S-wave time-shift anomalies below the elliptical reservoir is also reduced, indicating that the effective reservoir thickness closer to the endcaps becomes too small to be resolved by seismic waves. On the whole, P-wave time shifts are comparable to those for the rectangular reservoir, but PS- and S-wave shifts are slightly reduced. Hence, to accurately model PS- and S-wave response of pinch-outs or channels, it might be helpful to use an elliptical reservoir shape.

Time-shift perturbations caused by a mild (5°) tilt of the reservoir are illustrated in Figure 15g, 15h, and 15i. Tilt-induced rotations of the shear strains about the endcaps influence the deviatoric strain tensor, and cause a slight variation of P-wave time shifts above the reservoir. PS- and S-wave time shifts are still dominated by the velocity changes in the reservoir, and remain essentially unchanged. Tilt-related time-shift perturbations for all three wave types occur near the top and bottom of the reservoir and become insignificant at distances more than 300 m from it. This small perturbation does not warrant the use of tilted compartments for time-shift modeling and inversion, unless reservoir dip is significant or reflectors of interest are located in the immediate vicinity of the reservoir.

Discussion: Geomechanical complexity and magnitude of time shifts

The magnitudes of the two-way traveltime shifts shown in Figures 8, 9, 10, and 11 are higher than those typically observed in field data (Guilbot and Smith, 2002; Hatchell and Bourne, 2005; Herwanger et al., 2007; Hodgson et al., 2007; Rickett et al., 2007). Apart from differences due to the use of shot records rather than poststack migrated data, these disagreements may be caused by integration of rock physics and empirical data in the geomechanical modeling.

The effective stress coefficient (α) in equation 2 governs how the rock matrix and fluid within the reservoir volume determine the effective pressure (P_{eff}) in equation 3. At higher porosities, the aggregate bulk modulus (K_a) is dominated by fluid behavior. If K_a approaches the modulus of the grain material (K_g), α is close to unity. However, when production reduces porosity, K_a approaches zero, and P_{eff} reduces to the pressure of the overburden. While we have used an empirically determined value of $\alpha = 0.85$ for Berea sandstone, employing a variable effective stress coefficient that vanishes for large depressurization and compaction will mitigate changes in effective pressure. Hence, reducing α directly, or as a function of K_a (equation 2) due to changing fluid content or porosity, will result in smaller time shifts.

Integration of rock-physics data into time-shift modeling is complicated by disagreements between laboratory measurements and in situ values estimated from field data. For example, fractional changes in velocity with strain ("R-values") estimated from seismic data typically range from 1 to 5 (Hatchell and Bourne, 2005). In contrast, laboratory measurements yield R-values for similar rocks that exceed 700 (Bathija et al., 2009). Gurevich (2004) suggests that alternative estimates of effective stress/strain should be used when evaluating the elastic properties of rocks. The third-order stiffness coefficients of Berea sandstone measured by Sarkar et al. (2003) reflect the properties of their lab samples. However, their data set is small, and the measurements were made for stress-released (extracted), dry samples under uniaxial stress. Such laboratory conditions do not adequately represent triaxially stressed, saturated, in situ reservoir rocks. Further, Winkler and Liu (1996) state that third-order stiffness coefficients are only valid with respect to the measurement reference stress state, which is zero under laboratory conditions. Thus, the empirical third-order stiffnesses in our geomechanical models may be overstated, which may substantially increase the magnitude of estimated time shifts.

CONCLUSIONS

We described a processing methodology for estimating P-, S-, and PS-wave time shifts from full-waveform synthetic data generated by coupled geomechanical and seismic modeling. The processing flow includes *f-k* filtering of baseline and monitor shot records followed by cross-correlation skip corrections and adaptive polynomial fitting of time-shift curves. Our processing flow was used to study time-lapse signatures of a simple sandstone reservoir over a wide range of reservoir depths and pressure drops, including the individual contributions of both volumetric and deviatoric strain components.

P-wave time shifts measured from full-waveform data are generally close to those obtained in previous research using linearized traveltime equations and anisotropic ray tracing. The offset dependence of P-wave time shifts is largely influenced by compaction-induced anisotropy controlled by deviatoric strain, which produces non-negligible values of the parameter δ outside the reservoir. In addition, arching and "pull-up" zones near the top and bottom of the reservoir, which correlate with $\delta(x, z)$, cause the largest P-wave time shifts to occur for reflectors just above and below the reservoir. P-wave lags above the reservoir reach approximately 45 ms for the maximum depressurization (50%) and reservoir depth (2.5 km).

S-wave time shifts are largely determined by elevated deviatoric and volumetric strains inside the reservoir, which acts as a high-velocity lens. The contributions of both strain components to the time shifts of S-waves are nearly the same, with the total shift for reflectors beneath the reservoir being 2–3 times higher (up to 90 ms) than that of P-waves. In contrast, S-wave time shifts are much smaller above and to the sides of the reservoir. Compaction-induced SV-wave anisotropy is insignificant, which reduces the offset variation of S-wave time shifts.

PS-wave time shifts depend on the ray trajectory with respect to the reservoir. Outside the reservoir, the P-wave leg is primarily influenced by the deviatoric strains. Inside the reservoir, elevated deviatoric and volumetric strains generate significant P- and S-wave time shifts. The S-wave leg, however, incurs substantial time shifts only when it crosses the reservoir. For reflectors below the reservoir, PS-wave time shifts are approximately two times smaller than those of S-waves (up to 55 ms).

Elliptical reservoirs with the same aspect ratio as the modeled rectangular reservoir produce only minor variations of P-wave time-shift distributions and small reductions in PS- and S-wave time shifts below the reservoir. Likewise, a mild (5°) tilt of a rectangular reservoir causes only slight time-shift perturbations in the immediate vicinity of the reservoir. Therefore, time-shift analysis for many reservoirs embedded in horizontal or gently dipping layers may be accomplished using multi-compartment models comprised of rectangular blocks.

The time-shift distributions presented here have different implications for using each wave type in time-lapse studies. Because P-wave offset-dependent time shifts are sensitive to stress/strain-induced anisotropy, they yield useful information about deviatoric stress, especially for shot locations outside the lateral extent of the

reservoir. However, until significant reservoir depressurizations are achieved, P-wave time shifts and their offset variation may be too small to be reliably measured on field data. Although S-wave anisotropy is weak, larger PS- and S-wave time shifts for waves passing through the reservoir can be used to monitor geomechanical and pressure changes inside the reservoir volume. Our modeling agrees with empirical rock-physics observations that the shear-wave velocity (in particular V_{S0} inside the reservoir) is sensitive to effective pressure changes and the associated variations in stress and strain. PS-wave time shifts partially exhibit this sensitivity along with offset dependence of time shifts incurred on the P-wave leg. The distinct differences between the spatial distributions of P- and PS-wave time shifts outside the reservoir may be exploited to separate the individual contributions of the volumetric and deviatoric strains. Separation of the two is most important above the reservoir where the stress/strain anomalies interfere with drilling activities. The spatial distributions and relative magnitudes of time shifts for different wave types analyzed here should be helpful in designing monitor time-lapse surveys and inversion for reservoir pressure/stress changes.

ACKNOWLEDGMENTS

REFERENCES

Barkved, O. I., and T. Kristiansen, 2005, Seismic time-lapse effects and stress changes: Examples from a compacting reservoir: The Leading Edge, **24**, 1244–1248, doi: 10.1190/1.2149636.

Barton, N., 2006, Rock quality, seismic velocity, attenuation and anisotropy: Taylor & Francis.

Bathija, A. P., M. Batzle, and M. Prasad, 2009, An experimental study of the dilation factor: Geophysics, **74**, no. 4, E181–E191, doi: 10.1190/1.3137060.

Batzle, M., and D. Han, 2009, Rock and fluid properties: Seismic rock physics, SEG Continuing Education Series, Denver Geological Society.

Calvert, R., 2005, Insights and methods for 4D reservoir monitoring and characterization: Distinguished Instructor Short Course, SEG.

Christensen, N. I., and H. F. Wang, 1985, The influence of pore pressure and confining pressure on dynamic elastic properties of Berea sandstone: Geophysics, **50**, 207–213, doi: 10.1190/1.1441910.

COMSOL AB, 2008, COMSOL Multiphysics, http://www.comsol.com/.

Davis, R. O., and A. P. S. Selvadurai, 1996, Elasticity and geomechanics: Cambridge University Press.

Downs, J., and D. A. Faux, 1995, Calculation of strain distributions in multiple-quantum-well strained-layer structures: Journal of Applied Physics, **77**, 2444–2447, doi: 10.1063/1.358771.

Dusseault, M. B., S. Yin, L. Rothenburg, and H. Han, 2007, Seismic monitoring and geomechanics simulation: The Leading Edge, **26**, 610–620, doi: 10.1190/1.2737119.

Fjær, E., 2009, Static and dynamic moduli of a weak sandstone: Geophysics, **74**, no. 2, WA103–WA112, doi: 10.1190/1.3052113.

Fuck, R. F., A. Bakulin, and I. Tsvankin, 2009, Theory of traveltime shifts around compacting reservoirs: 3D solutions for heterogeneous anisotropic media: Geophysics, **74**, no. 1, D25–D36, doi: 10.1190/1.3033215.

Fuck, R. F., and I. Tsvankin, 2009, Analysis of the symmetry of a stressed medium using nonlinear elasticity: Geophysics, **74**, no. 5, WB79–WB87, doi: 10.1190/1.3157251.

Fuck, R. F., I. Tsvankin, and A. Bakulin, 2011, Influence of background heterogeneity on traveltime shifts for compacting reservoirs: Geophysical Prospecting, **59**, 78–89, doi: 10.1111/j.1365-2478.2010.00909.x.

Geertsma, J., 1973, Land subsidence above compacting oil and gas reservoirs: Journal of Petroleum Technology, **25**, 734–744, doi: 10.2118/3730-PA.

Guilbot, J., and B. Smith, 2002, 4-D constrained depth conversion for reservoir compaction estimation: Application to Ekofisk Field: The Leading Edge, **21**, 302–308, doi: 10.1190/1.1463782.

Gurevich, B., 2004, A simple derivation of the effective stress coefficient for seismic velocities in porous rock: Geophysics, **69**, 393–397, doi: 10.1190/1.1707058.

Hatchell, P., and S. Bourne, 2005, Rocks under strain: Strain-induced time-lapse time shifts are observed for depleting reservoirs: The Leading Edge, **24**, 1222–1225, doi: 10.1190/1.2149624.

Hearmon, R., 1953, 'Third-order' elastic coefficients: Acta Crystalographia, **6**, 331–340, doi: 10.1107/S0365110X53000909.

Herwanger, J., E. Palmer, and C. R. Schiøtt, 2007, Anisotropic velocity changes in seismic time-lapse data: 77th Annual International Meeting, SEG, Expanded Abstracts, 2883–2887.

Herwanger, J. V., and S. A. Horne, 2009, Linking reservoir geomechanics and time-lapse seismics: Predicting anisotropic velocity changes and seismic attributes: Geophysics, **74**, no. 4, W13–W33, doi: 10.1190/1.3122407.

Hodgson, N., C. MacBeth, L. Duranti, J. Rickett, and K. Niheil, 2007, Inverting for reservoir pressure change using time-lapse time strain: Application to Genesis Field, Gulf of Mexico: The Leading Edge, **26**, 649–652, doi: 10.1190/1.2737104.

Hofmann, R., X. Xu, M. Batzle, M. Prasad, A.-K. Furre, and A. Pillitteri, 2005, Effective pressure or what is the effect of pressure?: The Leading Edge, **24**, 1256–1260, doi: 10.1190/1.2149644.

Hu, S. M., 1989, Stress from a parallelepipedic thermal inclusion in a semi-space: Journal of Applied Physics, **66**, 2741–2743, doi: 10.1063/1.344194.

Landrø, M., 2001, Discrimination between pressure and fluid saturation changes from time lapse data: Geophysics, **66**, 836–844, doi: 10.1190/1.1444973.

Landrø, M., and J. Stammeijer, 2004, Quantitative estimation of compaction and velocity changes using 4D impedance and traveltime changes: Geophysics, **69**, 949–957, doi: 10.1190/1.1778238.

Lumley, D., 2001, Time-lapse seismic reservoir monitoring: Geophysics, **66**, 50–53, doi: 10.1190/1.1444921.

Lumley, D., D. Adams, R. Wright, D. Markus, and S. Cole, 2008, Seismic monitoring of CO_2 geo-sequestration: realistic capabilities and limitations: 78th Annual International Meeting, SEG, Expanded Abstracts, 2841–2845.

Lumley, D. E., 1995, Seismic time-lapse monitoring of subsurface fluid flow, SEP-91: Ph.D. thesis, Stanford University.

McCann, G. D., and C. H. Wilts, 1951, A mathematical analysis of the subsidence in the Long Beach-San Pedro area: Technical report, Caltech.

Minkoff, S. E., C. M. Stone, S. Bryant, and M. Peszynska, 2004, Coupled geomechanics and flow simulation for time-lapse seismic modeling: Geophysics, **69**, 200–211, doi: 10.1190/1.1649388.

Olden, P., P. Corbett, R. Westerman, J. Somerville, B. Smart, and N. Koutsabeloulis, 2001, Modeling combined fluid and stress change effects in the seismic response of a producing hydrocarbon reservoir: The Leading Edge, **20**, 1154–1163, doi: 10.1190/1.1486773.

Prasad, M., and M. H. Manghnani, 1997, Effects of pore and differential pressure on compressional wave velocity and quality factor in Berea and Michigan sandstones: Geophysics, **62**, 1163–1176, doi: 10.1190/1.1444217.

Prioul, R., A. Bakulin, and V. Bakulin, 2004, Nonlinear rock physics model for estimation of 3D subsurface stress in anisotropic formations: Theory and laboratory verification: Geophysics, **69**, 415–425, doi: 10.1190/1.1707061.

Rickett, J., L. Duranti, T. Hudson, B. Regel, and N. Hodgson, 2007, 4D time strain and the seismic signature of geomechanical compaction at Genesis: The Leading Edge, **26**, 644–647, doi: 10.1190/1.2737103.

Rickett, J., and D. Lumley, 2001, Cross-equalization data processing for time-lapse seismic reservoir monitoring: A case study from the Gulf of Mexico: Geophysics, **66**, 1015–1025, doi: 10.1190/1.1487049.

Roste, T., 2007, Monitoring overburden and reservoir changes from prestack time-lapse seismic data — Applications to chalk fields: Ph.D. thesis, Norwegian University of Science and Technology.

Sarkar, D., A. Bakulin, and R. L. Kranz, 2003, Anisotropic inversion of seismic data for stressed media: Theory and a physical modeling study on Berea sandstone: Geophysics, **68**, 690–704, doi: 10.1190/1.1567240.

Sarker, R., and M. Batzle, 2008, Effective stress coefficient in shales and its applicability to Eaton's equation: The Leading Edge, **79**, 798–804, doi: 10 .1190/1.2944167.

Sava, P., J. Yan, and J. Godwin, 2010, SFEWE elastic finite difference wave-propagation development code for the Madagascar seismic software collection: http://www.reproducibility.org.

Sayers, C. M., 2010, Geophysics under stress: Geomechanical applications of seismic and borehole acoustic waves, Distinguished Instructor Short Course: SEG.

Sayers, C. M., and P. M. Schutjens, 2007, An introduction to reservoir geomechanics: The Leading Edge, **26**, 597–601, doi: 10.1190/1 .2737100.

Sayers, C. M., M. J. Woodward, and R. C. Bartman, 2002, Seismic pore-pressure prediction using reflection tomography and 4-C seismic data: The Leading Edge, **21**, 188–192, doi: 10.1190/1.1452611.

Schutjens, P. M. T. M., T. H. Hanssen, M. H. H. Hettema, J. Merour, P. de Bree, J. W. A. Coremans, and G. Helliesen, 2004, Compaction-induced porosity/permeability reduction in sandstone reservoirs: Data and model for elasticity-dominated deformation: SPE Reservoir Evaluation & Engineering, **7**, 202–216, doi: 10.2118/88441-PA.

Scott, T. E., 2007, The effects of stress path on acoustic velocities and 4D seismic imaging: The Leading Edge, **26**, 602–608, doi: 10.1190/1 .2737101.

Sen, V., and A. T. Settari, 2005, Coupled geomechanical and flow modeling of compacting reservoirs: The Leading Edge, **24**, 1284–1286, doi: 10 .1190/1.2149657.

Shapiro, S. A., 2003, Elastic piezosensitivity of porous and fractured rocks: Geophysics, **68**, 482–486, doi: 10.1190/1.1567215.

Strehle, R., 1987, Subsidence in Long Beach: Presented at the AAPG Pacific Section — Oil Producing Areas in Long Beach.

Tsvankin, I., 2005, Seismic signatures and analysis of reflection data in anisotropic media, 2nd ed.: Elsevier Science.

Whitley, P. K., 1992, The geology of Heidrun, A giant oil and gas field on the Mid-Norwegian shelf, *in* M. T. Halbouty, ed., Giant oil and gas fields of the decade 1978–1988: AAPG, **54**, 383–406.

Winkler, K. W., and X. Liu, 1996, Measurements of third-order elastic constants in rocks: Journal of the Acoustical Society of America, **100**, 1392–1398, doi: 10.1121/1.415986.

Xu, X., R. Hofmann, M. Batzle, and T. Tshering, 2006, Influence of pore pressure on velocity in low-porosity sandstone: Implications for time-lapse feasibility and pore-pressure study: Geophysical Prospecting, **54**, 565–573, doi: 10.1111j.1365-2478.2006.00569.x.

Yale, D. P., and W. H. Jamieson, 1994, Static and dynamic mechanical properties of carbonates: *in* P. P. Nelson, and S. E. Laubach, eds., Proceedings of the 1st North American Rock Mechanics Symposium, Balkema, 463–471.

Zoback, M. D., 2007, Reservoir geomechanics: Cambridge University Press.